

Quantum Anomalous Hall Effect in 2D Organic Topological Insulators

Z. F. Wang, Zheng Liu, and Feng Liu*
*Department of Materials Science and Engineering,
 University of Utah, Salt Lake City, UT 84112, USA*

Quantum anomalous Hall effect (QAHE) is a fundamental transport phenomenon in the field of condensed-matter physics. Without external magnetic field, spontaneous magnetization combined with spin-orbit coupling give rise to a quantized Hall conductivity. So far, a number of theoretical proposals have been made to realize the QAHE, but all based on *inorganic* materials. Here, using first-principles calculations, we predict a family of 2D *organic* topological insulators (OTIs) for realizing the QAHE. Designed by assembling molecular building blocks of triphenyl-transition-metal compounds into a hexagonal lattice, this new classes of organic materials are shown to have a nonzero Chern number and exhibit a gapless chiral edge state within the Dirac gap.

PACS numbers: 73.43.-f, 72.20.-i, 81.05.Fb, 72.80.Le

The Hall effect describes a transverse voltage appearing when electric current flows in a conductor subject to a perpendicular magnetic field [1]. The quantum Hall effect refers to the quantized Hall conductivity due to Landau quantization, as observed in a 2D electron system [2]. The essential ingredient to produce the Hall effect is to break the time-reversal symmetry. As such, external magnetic field is not the only way to realize this effect. An interesting alternative is to have the internal magnetization coupled with spin-orbit coupling (SOC) that can also break time-reversal symmetry, leading to the Hall effect without applying external magnetic field [3]. This is called anomalous Hall effect (AHE), which was first observed in ferromagnetic metals in 1881 [4].

Similar to the Hall effect, the AHE was also expected to have its quantized counterpart, the quantum AHE (QAHE). The QAHE was first proposed by Haldane [5] in a honeycomb lattice within a staggered magnetic field, in which the time-reversal symmetry is broken, but the net magnetic flux is zero. Subsequently, some realistic materials were theoretically proposed to realize the QAHE, such as mercury-based quantum wells [6], graphene [7–9] and topological insulators (TIs) [10]. In general, in a QAHE material, internal magnetism, such as the one induced by transition metals, breaks the time-reversal symmetry and splits the spin degenerated bands. In addition, the SOC opens a global band gap, giving rise to a topologically nontrivial insulating state characterized with the quantized Hall conductivity.

Despite the theoretical progress, due to the difficulty in controlling magnetization and SOC, the QAHE has yet to be observed experimentally [11, 12]. So far, all the theoretical proposals for realizing the QAHE are based on inorganic materials. It is fascinating to note that many fundamental physical phenomena in inorganic materials and devices have always found their way to organic counterparts, such as the organic superconductors [13], light-emitting diodes [14], solar cells [15] and field-effect transistors [16]. Generally, organic materials have the added advantages of low cost, easy fabrication and mechanical flexibility. Therefore, an interesting question is whether the QAHE can be realized in organic materials.

Recently, we have demonstrated that 2D OTI can be

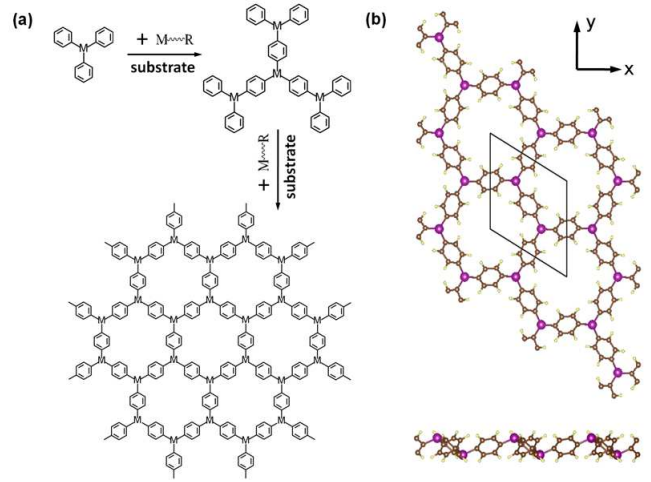


Figure 1: Schematic illustration of the 2D organometallic lattice. (a) The proposed synthesis process from the triphenyl-transition-metal molecules to the 2D organometallic lattices. R is a functional group attached to the transition metal atom. (b) Top and side view of the optimized structure of the 2D TMn lattice. Solid rhombus shows the unit cell.

realized by self-assembly of triphenyl-metal molecules into a hexagonal lattice [17], provided the metal elements have a large SOC, such as Pb, Bi, and In. Without the SOC, such organic lattices give a Dirac-cone state with zero gap; turning on the SOC, a topologically nontrivial gap opens at the Dirac point and a 1D gapless Dirac edge state rises within the nontrivial gap. Naturally, if such lattices are magnetized with the inclusion of transition metal elements, QAHE may be expected.

In this Letter, we demonstrate that QAHE can indeed be realized in 2D OTI self-assembled from triphenyl-transition-metal compounds, using triphenyl-manganese (TMn) as a model system. Based on Chern number and edge state calculations, we confirm the 2D TMn lattice have nontrivial topological Dirac-gap states and explain the physical origin of its QAHE due to both the strong magnetization and SOC provided by Mn atoms. Our findings open a new theoretical branch

for studying the QAHE in organic materials, which will greatly broaden the scientific impact of the QAHE.

To examine the band structures and topological properties of 2D organometallic lattices made of TMn [$\text{Mn}(\text{C}_6\text{H}_5)_3$] molecules, first-principles calculations were carried out in the framework of the PBE-GGA functional using the VASP package [18]. All self-consistent calculations were performed with a plane-wave cutoff of 500 eV on a $7 \times 7 \times 1$ Monkhorst-Pack k-point mesh. Supercell with a vacuum layer more than 15 Å thick is used to ensure decoupling between neighboring slabs. For structural relaxation, all the atoms are allowed to relax until atomic forces are smaller than 0.01 eV/Å.

The TMn molecule consists of a Mn atom bonded with three benzene rings with three-fold rotational symmetry. When bridged with a Mn atom, they naturally form a 2D hexagonal lattice, as shown in Fig. 1. Figure 1 is not a calculation of the actual chemical reaction (which would be computationally too demanding) but only a proposed synthesis process for obtaining the TMn lattice. There are two Mn atoms and three benzene rings with a chemical formula of $\text{Mn}_2\text{C}_{18}\text{H}_{12}$ in each unit cell and the neighboring benzene rings are bridge-bonded through the para-Mn atoms. The optimized 2D lattice is buckled with the para-Mn atoms moving alternately up and down out of the plane of benzene rings (see Fig. 1b). In addition, each benzene rotated slightly along the Mn-Mn axis in a clockwise manner. The equilibrium lattice constant (L) is found to be 10.7 Å with the Mn-Mn distance and height difference being 6.45 Å and 1.86 Å, respectively.

First, we analyse the band structure of TMn lattice purposely without SOC, but with magnetization. Our results shown that the ground state of TMn lattice is ferromagnetic (the ferromagnetic state is found 0.18 eV lower than the anti-ferromagnetic state), and its magnetic moment is $4\mu_B$ per unit cell. This is because the 3d-shell of Mn is half filled, it can provide three d electrons to bond with the C. Consequently, each Mn atom has two d electrons left. Based on the Hund's rule, all the 3d electrons prefer to be equally spin polarized showing a maximum magnetization. So the two Mn atoms in the unit cell have four d electrons with the same spin. The corresponding band structure of this ferromagnetic state is shown in Fig. 2(a). Due to the internal magnetization induced exchange field, the spin-up (red dashed line) and spin-down (blue solid line) bands are completely split away from each other, and only the spin-down component is left around the Fermi level. Magnifying the bands around the Fermi level, we can see a clear linear Dirac band, with the Fermi level located exactly at the Dirac point (K and K'), as shown in Fig. 2(c). Similar Dirac bands for the spin-up components can also be found below the Fermi level.

Next, both the magnetization and SOC are included in the calculation, and the corresponding band structure of the TMn lattice is shown in Fig. 2(b). Our magnetic anisotropy calculation shown that the SOC

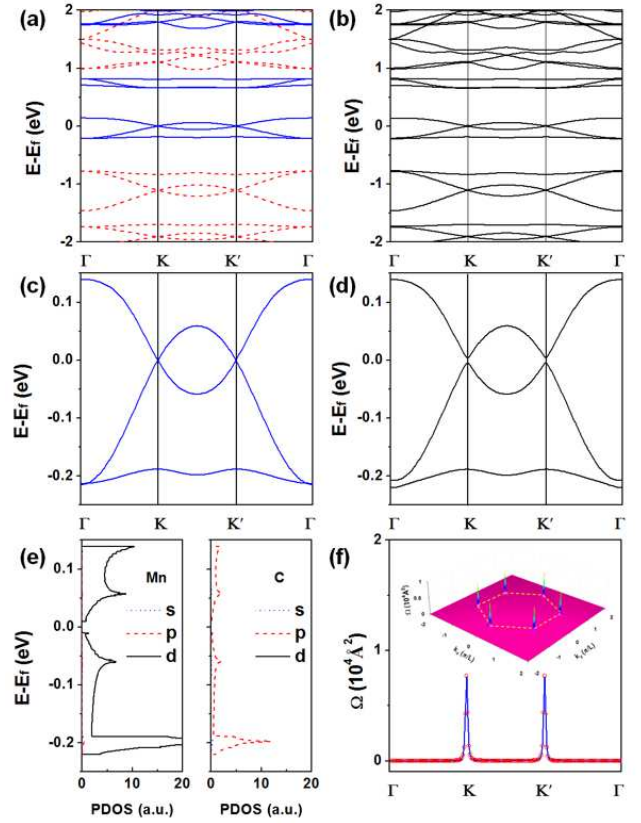


Figure 2: (a) Band structures of the TMn lattice by including magnetization without SOC. Red dashed lines and blue solid lines denote spin-up and spin-down bands, respectively. (b) Band structures of the TMn lattice by including SOC. (c) and (d) Magnification of the band structures around the Fermi level for (a) and (b), respectively. (e) Projected density of states around the Fermi level for the TMn lattice with SOC. (f) Berry curvature for the whole valence bands (blue solid line) and the first valence band below the Fermi level (red open circle) along the high symmetry directions. The inset is the 2D distribution of berry curvature for the whole valence bands in the momentum space. The first Brillouin zone is denoted by the dashed line and two inequivalent valleys are labeled as K and K' .

ground state has the out-of-plane spin orientation, which is 0.5 meV lower than the in-plane spin orientation. Comparing the band structures without [Fig. 2(a)] and with SOC [Fig. 2(b)], we found that their band structures are almost the same, except a sizable bulk band gap (9.5 meV) opened at the K and K' Dirac points, which can be seen from the magnified bands in Fig. 2(d), and the Fermi level lies just inside the Dirac gap. We also checked the orbital components around the Dirac gap. As shown in Fig. 2(e), the Dirac states mainly come from the d orbit of Mn atoms, and the p orbit of C atoms has little contribution. Therefore, the Dirac band around the Fermi level originated from the hexagonal Mn lattice, which also introduces the SOC to open the Dirac gap.

To identify the nontrivial topological properties of the Dirac gap in TMn lattice and prove the existence of QAHE in such magnetized OTI, we further calculated

the Berry curvature in the TMn lattice. The Berry curvature (Ω) can be obtained using the Kubo formula [19, 20],

$$\Omega(\mathbf{k}) = \sum_n f_n \Omega_n(\mathbf{k}),$$

$$\Omega_n(\mathbf{k}) = - \sum_{n' \neq n} 2Im \frac{\langle \psi_{n\mathbf{k}} | v_x | \psi_{n'\mathbf{k}} \rangle \langle \psi_{n'\mathbf{k}} | v_y | \psi_{n\mathbf{k}} \rangle}{(\varepsilon_{n'\mathbf{k}} - \varepsilon_{n\mathbf{k}})^2}, \quad (1)$$

where n is the band index, $\varepsilon_{n\mathbf{k}}$ and $\psi_{n\mathbf{k}}$ are eigenvalue and eigenstate of band n , $v_{x/y}$ is the velocity operator, f_n is Fermi distribution function and the summation is over all the valence bands below the Fermi level. We have used the maximally localized Wannier functions (MLWFs) to calculate the Berry curvature by using the Wannier90 package [21]. The Berry curvature for the whole valence bands (blue solid line) along the high symmetry directions and the corresponding 2D distribution in momentum space are shown in Fig. 2(f) and its inset, in which we can see that the nonzero Berry curvatures are mainly localized around K and K' points with the same sign. Integrating the Berry curvatures over the first Brillouin zone, we can obtain the Chern number, $C = \frac{1}{2\pi} \int_{BZ} d^2k \Omega$, which can be used to characterize the quantum Hall conductivity. A nonvanishing Chern number in the absence of the external magnetic field is a signature of the QAHE. Our calculated Chern number is $C = 1$, *i.e.*, each Dirac cone's (K and K') contribution is 0.5, which indeed confirms the QAHE in the TMn lattice.

Since our TMn lattice has inversion symmetry, the gap opening at the Dirac point cannot be induced by the Rashba SOC, but instead by the intrinsic SOC of Mn atoms. To further illustrate the intrinsic SOC effect, we write a single π -band tight-binding (TB) model to describe the Dirac bands of TMn lattice. To the first-order approximation, the TB Hamiltonian of the hexagonal TMn lattice with exchange field and intrinsic SOC can be written as,

$$H = t \sum_{\langle i,j \rangle, \alpha} c_{i\alpha}^+ c_{j\alpha} - M \sum_{i, \alpha, \beta} c_{i\alpha}^+ s_{\alpha\beta}^z c_{i\beta}$$

$$+ \lambda_{so} \frac{2i}{\sqrt{3}} \sum_{\langle\langle i,j \rangle\rangle} c_i^+ \vec{s} \cdot (\vec{d}_{kj} \times \vec{d}_{ij}) c_j \quad (2)$$

Here, $c_{i\alpha}^+$ and $c_{i\alpha}$ are π -band creation and annihilation operators for an electron with spin α on site i . The first term is the nearest-neighbor hopping with magnitude t . The second term is the exchange field with magnitude M . The third term is the next-nearest-neighbor intrinsic SOC with amplitude λ_{so} , \vec{s} is the spin Pauli matrix, \vec{d}_{kj} is the unit vector pointing from site j to k . In our numerical calculation, the 4×4 reciprocal-space Hamiltonian matrix of Eq. (2) is written in the basis $\{\psi_{A\uparrow}, \psi_{A\downarrow}, \psi_{B\uparrow}, \psi_{B\downarrow}\}$.

By diagonalizing the above Hamiltonian in reciprocal space, we obtain its band structure, as shown in Fig. 3. In our calculation, all the parameters are scaled with the hopping parameter t . Without the intrinsic

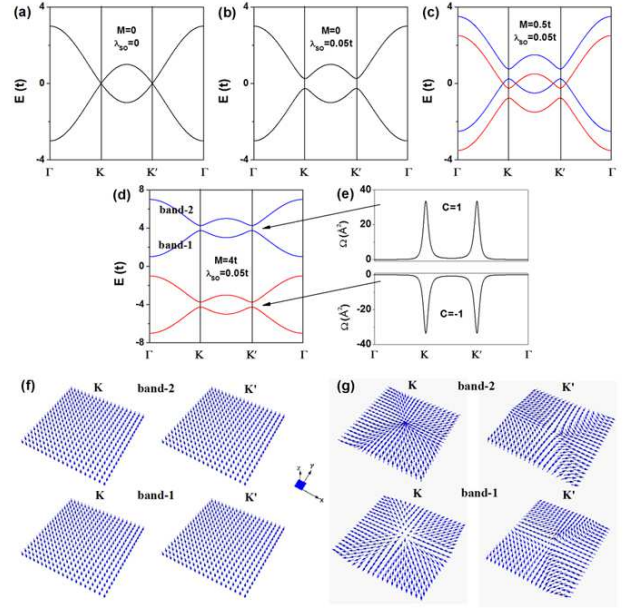


Figure 3: TB Band structure with (a) $M=0$ and $\lambda_{so}=0$, (b) $M=0$ and $\lambda_{so}=0.05t$, (c) $M=0.5t$ and $\lambda_{so}=0.05t$ and (d) $M=4t$ and $\lambda_{so}=0.05t$. (e) Berry curvatures by setting the Fermi level within the intrinsic SOC gap indicated by the arrows and the resulting Chern numbers. Red (blue) color denotes spin-up (spin-down) bands. (f) and (g) Spin and pseudo-spin textures around K and K' for band-1 and band-2 shown in (d).

SOC and exchange field, the corresponding band structure along the high symmetry directions is shown in Fig. 3(a), where we can see the linear Dirac bands at K and K' points. When we turn on the intrinsic SOC but without the exchange field, a band gap is opened at the Dirac points, as shown in Fig. 3(b). Without the exchange field, all the bands are spin degenerated in Fig. 3(b). When we turn on both intrinsic SOC and exchange field, the spin degenerated bands are split. If the exchange field is large enough to overcome the intrinsic SOC gap, the spin-up (red line) and spin-down (blue line) bands will cross over with each other, as shown in Fig. 3(c). The situation here, however, is different from the case of Rashba SOC, there is no SOC gap opening at the band crossing points with different spins in the physical regime of small magnetization. However, if we further increase the exchange field, the spin-up and spin-down bands will completely separate from each other, as shown in Fig. 3(d), which corresponds to our case of TMn lattice. Then, we have a global gap induced by intrinsic SOC, leading to QAHE. To further check the topological properties of the gap states induced by intrinsic SOC, we calculated the Berry curvature by setting the Fermi level at the spin-up and spin-down Dirac gap, respectively (The real TMn lattice has the Fermi level in the gap of spin-down bands). The corresponding Berry curvature and Chern number are shown in Fig. 3(e). We found the non-zero Berry curvature that localizes around the Dirac point and the $C = -1$ ($C = 1$) for spin-up (spin-down) bands, con-

sistent with our first principles calculations. Thus, we confirm that the intrinsic SOC in TMn lattice is responsible for gap opening to realize the QAHE.

Besides realizing the QAHE in a new organic molecular lattice, it is also important to point out some new physics in our system in comparison with previous works. The QAHE in our proposed TMn lattice is induced by intrinsic SOC taking place in the strong magnetization regime with an odd Chern number ($C = 1$), while the QAHE in the graphene doped with 3d [7, 8] and 5d transition metals [9] is induced by Rashba SOC taking place in the weak magnetization regime with an even Chern number ($C = 2$). It was shown that the d-states in 5d transition metals doped graphene plays an important role in realizing the QAHE and there exists also a global Dirac gap between the bands of the same spin [Fig. 2(c) in Ref. 9], but it is 0.27 eV below the Fermi level and its Chern number is even ($C = -2$). We note that around the Dirac gap where Fermi energy is located, the π -bands are composed of d-orbitals in our TMn lattice but p-orbitals in the doped graphene.

In order to get a qualitative understanding about the Chern number value $C = 1$, the Berry curvature for the highest occupied valence band (VB) below the Fermi level is calculated, as shown in Fig. 2(f) (red open circle), which completely matches the total Berry curvature curve. This indicates that the total Chern number for other valence bands below the highest occupied valence band is zero. Thus, in the following, we focus on the highest occupied valence band only, and examine its spin components around the Dirac gap. As a comparison, the lowest unoccupied conduction band (CB) above the Fermi level is also studied. As shown in Fig. 4(a), the spin textures for VB and CB are uniformly pointing along the $-z$ direction around K and K' , as both come from the spin-down bands. Qiao *et al.* [8] recently showed that such spin texture has no contribution to the Chern number, but the pseudo-spin texture of the Dirac states will contribute to the Chern number.

To reveal the difference between spin and pseudo-spin, we calculate the Chern number (topological charge) resulting from the spin and pseudo-spin texture separately, using the TB model. The spin and pseudo-spin components are defined as [8] $\langle s_i \rangle = \langle \psi | I \otimes s_i | \psi \rangle$ and $\langle \sigma_i \rangle = \langle \psi | \sigma_i \otimes I | \psi \rangle$, respectively, where I is a 2×2 identity matrix, s_i (σ_i) is the spin (pseudo-spin) Pauli matrix with $i = x, y, z$ and $|\psi\rangle$ is the eigenvector of Eq. (2) in reciprocal space. Here, we choose the spin-down bands labeled with band-1 and band-2 in Fig. 3(d) for our calculation, as our first-principles calculations show only spin-down bands at the Fermi Level [Fig. 2(a)]. Fig. 3(f) shows the TB spin texture with all spins uniformly point along the $-z$ direction, consistent with the first-principles results [see Fig. 4(a)]. However, the pseudo-spin texture is not uniform, as shown in Fig. 3(g). Its in-plane components have different patterns depending on the valleys (K and K') and bands (band-1 and band-2), while its out-of-plane components only exist near the valley and point along either $-z$ or z direction. The spin and

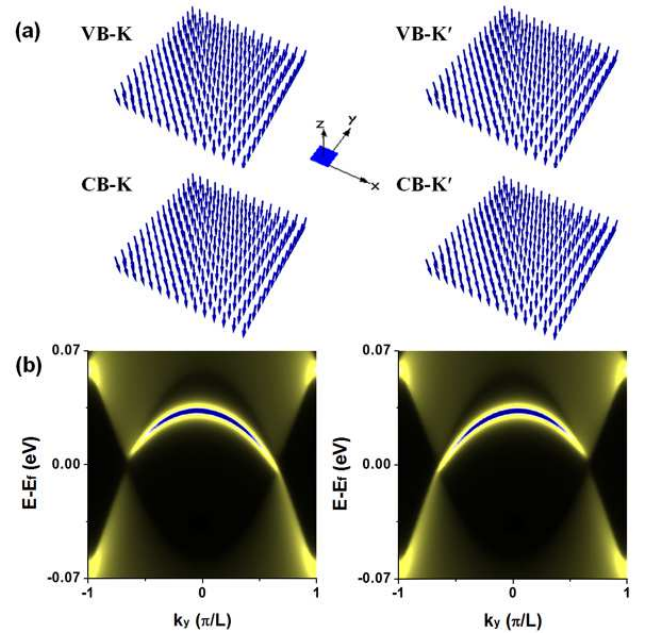


Figure 4: (a) Spin texture round K and K' for the highest occupied valence band and the lowest unoccupied conduction band. (b) Left and right semi-infinite edge states inside the Dirac gap of the TMn lattice.

pseudo-spin Chern number can be calculated as [8, 22] $n = 1/4\pi \int dk^2 (\partial_{k_x} \hat{\mathbf{h}} \times \partial_{k_y} \hat{\mathbf{h}}) \cdot \hat{\mathbf{h}}$, where $\hat{\mathbf{h}} = \mathbf{h}/|\mathbf{h}|$ with \mathbf{h} representing the projection of Hamiltonian in Eq. (2) into spin or pseudo-spin space. Physically, the unit vector $\hat{\mathbf{h}}$ represents the expectation value of the orientation of the spin or pseudo-spin associated with the eigenvector $|\psi\rangle$. For band-1 in Fig. 3(d), we found $n_{spin}=0$ and $n_{pseudo} = 0.5$ for both valleys. The pseudo-spin texture provides a half topological charge, corresponding to a meron. Thus, by counting two valleys' contribution, the Chern number will be $C = 1$. In addition, the sign of the topological charge is determined by the details of the pseudo-spin texture. For band-2 in Fig. 3(d), we found $n_{spin}=0$ and $n_{pseudo} = -0.5$ for both valleys. Therefore, the total Chern number for band-1 and band-2 is zero, which is consistent with our first-principles result by setting the Fermi level within the gap just above the lowest unoccupied conduction band.

The nonzero Chern number can also be manifested by the presence of chiral edge states within the topological nontrivial Dirac gap, so we now turn our attention to the edge state properties of the TMn lattice. By using the MLWFs obtained from the first-principles calculation, the edge Green's function [23] of the semi-infinite TMn lattice is constructed and the local density of state (LDOS) of edge states are calculated [17]. This method provides a direct connectivity between the edge states and the bulk states. Here, the semi-infinite TMn lattice is periodic along the y direction (parallel to the edge), and the left and right edges have the symmetric structure, as shown in Fig. 1(b). The LDOS of the left and right edge states are shown in Fig. 4(b), respectively, where one can clearly see one chiral gapless edge

state connecting the valence and conduction band with the same in-plane spin vortex. The left and right edge states have the symmetric structure, but with opposite group velocity, *i.e.*, they will propagate in opposite directions at different edges. The number of the edge states indicates the absolute value of the Chern number. Therefore, the one chiral edge state observed in the Dirac gap is consistent with our calculated Chern number $C = 1$.

Lastly, one critical point is whether the topological properties of TMn lattice can remain on a substrate. Naturally one should look for a substrate with minimal interfacial interaction with the TMn lattice. To test out this possibility, we have placed the TMn lattice on top of graphene [Fig. S1(a)] [24], which is expected to have a weak van der Waals interfacial interaction and right hexagonal symmetry. Our calculations show that because of lattice mismatch, the TMn lattice becomes a flat structure instead of the freestanding buckled structure, but the main features of QAHE remain intact. There is still a SOC gap at the Dirac point around Fermi level [Figs. S1(e) and (f)], within which a nontrivial topological edge state resides [Fig. S1(g)]. These results demonstrate the feasibility of attaining the QAHE of TMn lattice on a substrate. More details of the substrate calculations are given in the supplemental materials [24].

In summary, we have designed a new family of organometallic lattices for realizing the QAHE in magnetic OTIs. Molecular building blocks, with both strong magnetism and SOC, are assembled into a hexagonal lattice. Magnetization induced exchange field completely splits the spin-degenerated bands, so that the SOC opens a globe Dirac gap. Chern number and edge state calculations confirm the nontrivial topological properties of the Dirac gap, demonstrating the QAHE. Future investigations of similar OTIs using different transition metal elements and molecular ligands will further expand the scope of present study.

This work was supported by US DOE-BES (Grant No. DE-FG02-04ER46148) and NSF MRSEC (Grant No. DMR-1121252). Z.F.W. acknowledges additional support from ARL (Cooperative Agreement No. W911NF-12-2-0023). We thank the CHPC at University of Utah and NERSC for providing the computing resources.

* Corresponding author. E-mail: fliu@eng.utah.edu

- [1] E. H. Hall, *Amer. J. Math.* **2**, 287 (1879).
- [2] K. V. Klitzing *et al.*, *Phys. Rev. Lett.* **45**, 494 (1980).
- [3] N. Nagaosa *et al.*, *Rev. Mod. Phys.* **82**, 1539 (2010).
- [4] E. H. Hall, *Philos. Mag.* **12**, 157 (1881).
- [5] F. D. M. Haldane, *Phys. Rev. Lett.* **61**, 2015 (1988).
- [6] C.-X. Liu *et al.*, *Phys. Rev. Lett.* **101**, 146802 (2008).
- [7] Z. Qiao *et al.*, *Phys. Rev. B* **82**, 161414(R) (2010).
- [8] Z. Qiao *et al.*, *Phys. Rev. B* **85**, 115439 (2012).
- [9] H. Zhang *et al.*, *Phys. Rev. Lett.* **108**, 056802 (2012).
- [10] R. Yu *et al.*, *Science* **329**, 61 (2010).
- [11] C.-Z. Chang *et al.*, arXiv:1108.4754v1.
- [12] J. G. Checkelsky *et al.*, *Nature Phys.* **8**, 729 (2012).
- [13] D. Jérôme *et al.*, *J. Phys. Lett. (Paris)* **41**, L95 (1980).
- [14] C. W. Tang and S. A. Vanslyke, *Appl. Phys. Lett.* **51**, 913 (1987).
- [15] D. Kearns and M. Calvin, *J. Chem. Phys.* **29**, 950 (1958).
- [16] H. Koezuka, A. Tsumura and T. Ando, *Synth. Met.* **18**, 699 (1987).
- [17] Z. F. Wang *et al.*, *Nature Commun.* (doi:10.1038/ncomms2451); Z. Liu *et al.* arXiv:1210.1826v2.
- [18] G. Kresse and J. Hafner, *Phys. Rev. B* **47**, 558 (1993).
- [19] D. J. Thouless *et al.*, *Phys. Rev. Lett.* **49**, 405 (1982).
- [20] Y. Yao *et al.*, *Phys. Rev. Lett.* **92**, 037204 (2004).
- [21] A. A. Mostofi *et al.*, *Comput. Phys. Commun.* **178**, 685 (2008).
- [22] E. Prada *et al.*, *Solid State Comm.* **151**, 1075 (2011).
- [23] M. P. Lopez Sancho *et al.*, *J. Phys. F* **15**, 851 (1985).
- [24] See Supplemental Material at the http://link.aps.org/supplemental/**/ for more information on the substrate effect.